ACCSCIENCE PUBLISHING

International Journal of Bioprinting

RESEARCH ARTICLE

3D-printed perfusable tumor model for evaluating perfusion and chemotherapeutic response in ovarian cancer cells

Md Shahriar[1], Marielena Molinares[1], Ganesh Acharya[2], Komaraiah Palle[2], and Changxue Xu[1]*

[1]Department of Industrial, Manufacturing, and Systems Engineering, Edward E. Whitacre Jr. College of Engineering, Texas Tech University, Lubbock, Texas, USA

[2]Department of Cell Biology and Biochemistry, School of Medicine, Texas Tech University Health Sciences Center, Lubbock, Texas, USA

Abstract

Understanding the role of perfusion and chemotherapeutic response in solid tumors requires advanced *in vitro* models that closely recapitulate the tumor microenvironment. Addressing this need, we developed a perfusable three-dimensional (3D) gelatin methacrylate (GelMA)-based tumor model embedded with a hollow microchannel to investigate spatial variations in SKOV3 ovarian cancer cell behavior and their response to carboplatin. This study aims to overcome the limitations of conventional two-dimensional and non-perfused 3D cultures by introducing controlled perfusion and directional drug delivery, thereby providing a more physiologically relevant platform for cancer research and drug testing. Using extrusion- and inkjet-based bioprinting, SKOV3 cells were cultured within the GelMA matrix and exposed to continuous medium flow. We observed that cell behavior varied significantly with distance from the perfusion channel. Cells closer to the channel (0–300 μm) showed increased elongation (aspect ratio: 3.5), faster migration (28.98 μm/day), higher viability (96%), and elevated proliferation (index: 3.8), which progressively declined with increasing distance. Upon carboplatin exposure (0–50 μM), SKOV3 cells exhibited dose-dependent reductions in viability, proliferation, migration, and elongation, with the aspect ratio dropping to 1.17 and the viability to 5% at 50 μM. Matrix degradation analysis revealed increased pore enlargement under perfusion (87–190 μm), suggesting higher matrix metalloproteinase activity. This perfused 3D model enables precise evaluation of chemotherapeutic efficacy and tumor cell heterogeneity, offering a powerful tool for preclinical drug screening, tumor biology research, and future integration of vascular and immune components.

Keywords: Carboplatin chemotherapy; Cell migration; Drug resistance; Drug screening platform; Ovarian cancer cell; Perfusable three-dimensional tumor model; Three-dimensional bioprinting

***Corresponding author:**
Changxue Xu
(changxue.xu@ttu.edu)

Citation: Shahriar M, Molinares M, Acharya G, Palle K, Xu C. 3D bioprinting of a perfusable tumor microenvironment model to investigate perfusion and chemotherapeutic responses in ovarian cancer cells. *Int J Bioprint*. 2025;11(6):260-278. doi: 10.36922/IJB025320316

Received: August 7, 2025
1st revised: September 3, 2025
2nd revised: September 19, 2025
Accepted: September 22, 2025
Published online: September 23, 2025

1. Introduction

Metastasis remains the leading cause of cancer-related mortality, accounting for approximately 90% of cancer deaths across various tumor types.[1] This complex,

multifactorial process involves the detachment of malignant cells from the primary tumor, local invasion of adjacent tissues, and dissemination through the vasculature to distant organs.[2] The tumor microenvironment (TME), comprising extracellular matrix (ECM) components, stromal cells, biochemical gradients, and mechanical cues, plays a pivotal role in promoting tumor heterogeneity, invasion, and therapeutic resistance.[3] Understanding these intricate cellular behaviors requires model systems that recapitulate the three-dimensional (3D) architecture, biochemical gradients, and dynamic fluidic conditions found *in vivo*.[4]

Although widely used in cancer research, conventional two-dimensional monolayer cultures fail to replicate key physiological characteristics of the native TME. These systems lack the structural complexity, mechanical cues, and spatial organization that influence cell polarity, differentiation, and intercellular communication.[5] They also do not account for critical factors such as interstitial flow, oxygen and nutrient gradients, and shear stress, which play essential roles in tumor progression and treatment response. As a result, drug testing in two-dimensional models often overestimates therapeutic efficacy due to uniform drug exposure and the absence of diffusion barriers and ECM-mediated signaling found *in vivo*.[6] The simplified environment masks important mechanisms of drug resistance, including variable cell–matrix interactions and regional heterogeneity in drug penetration. To overcome these limitations, 3D culture systems have been developed to mimic the TME more accurately. Recent advancements in 3D tumor modeling have introduced diverse platforms, including multicellular tumor spheroids, patient-derived organoids, microfluidic systems, and bioprinted constructs. While multicellular tumor spheroids offer scalability for drug screening and patient-derived organoids preserve patient-specific tumor characteristics, both lack integrated perfusion, limiting nutrient and oxygen delivery, and resulting in necrotic cores and incomplete TME mimicry.[7] Microfluidic devices address this by introducing dynamic flow but offer limited spatial complexity. In contrast, 3D bioprinting enables precise spatial control and the fabrication of perfusable vascular structures, closely replicating *in vivo* physiological gradients and shear stress.[8] This enhances cancer cell proliferation, drug response, and metastasis modeling. Among hydrogel scaffolds used, gelatin and its methacrylated derivative, gelatin methacrylate (GelMA), are particularly advantageous. Derived from collagen, they mimic key characteristics of the ECM, including cell-binding motifs (i.e., Arg-Gly-Asp sequences) and matrix metalloproteinase (MMP)-sensitive degradation sites, both of which originate from the parent collagen and inherently support cell adhesion and proliferation.[9] Furthermore, GelMA's tunable stiffness and photo-crosslinkability make it suitable for constructing biomimetic, perfusable TMEs with high fidelity, and translational relevance. While gelatin alone can form hydrogels (often enzymatically crosslinked with microbial transglutaminase [TG]), this process takes hours for bulk models.[10] Such a long curing time would greatly prolong fabrication, leaving cells suspended in a liquid environment and potentially disrupting the 3D tumor architecture before solidification. Moreover, prolonged ultraviolet crosslinking time for GelMA can significantly decrease cell viability in a time-dependent manner.[9] Therefore, we adopted an innovative two-step crosslinking approach in which gelatin supplementation and a secondary TG crosslink enabled shorter ultraviolet curing of the GelMA–gelatin construct, thereby enhancing cell viability. Furthermore, we fabricated the hollow perfusable channel via sacrificial bioprinting of Pluronic F-127, enabling precise lumen positioning and clean removal within the 3D construct, yielding smooth, patent conduits suitable for reliable perfusion.

Several researchers have investigated the behavior of cancer cells using 3D perfusable tumor models to understand mechanisms of drug response and resistance. For instance, Wang *et al.*[11] developed a perfusable 3D brain tumor co-culture model using polyethylene glycol hydrogels and alginate microfibers with patient-derived glioblastoma cells, enhancing tumor cell proliferation. Ertekin *et al.*[12] utilized alginate–gelatin scaffolds containing breast cancer aggregates and established cell morphology as a malignancy indicator within 3D models. Their findings suggest that confinement and mechanical stress, rather than hypoxia, drive the formation of multinucleated cells, potentially contributing to drug resistance within the artificial TME.[12] More recently, a 3D-bioprinted tumor mimic by Maggiotto *et al.*[13] used GelMA and Pluronic F-127 with neuroblastoma cells to achieve a perfusable TME model, showing enhanced cell viability and metastatic mimicry. Moreover, a key focus on current 3D cancer modeling involves investigating drug resistance and diverse cellular responses to chemotherapy. Hong *et al.*[14] utilized 3D-bioprinted spheroids of HeLa, HepG2, and A549 cells to model multidrug resistance against doxorubicin, revealing that 3D cultures exhibited greater resistance proportional to their transporter protein levels. Similarly, a study from Fang *et al.*[15] employed a microarray device for 3D patient-derived breast cancer organoids to examine adriamycin resistance, noting significant heterogeneity in drug response between naïve and resistant organoid groups. While these studies have advanced our understanding of drug sensitivity in cancer

cells, accurately replicated functional perfusable structures that closely resemble the native TME are still lacking.

This study presents a perfusable 3D GelMA–gelatin tumor model to investigate spatial gradients and chemotherapeutic response in SKOV3 ovarian cancer cells. A sacrificially patterned microchannel enabled continuous medium flow, mimicking physiological perfusion, and nutrient delivery. The model revealed distinct differences in drug sensitivity and adaptive behavior, influenced by proximity to the perfusion channel. By integrating ECM-mimetic scaffolds with dynamic flow, this platform offers a physiologically relevant system for studying tumor progression, drug resistance, and microenvironmental regulation *in vitro*.

2. Materials and methods

2.1. Ink preparation

In this study, a mixture of GelMA and gelatin was selected as the bioink formulation to replicate the ECM environment and serve as a cell carrier, as they contain cell-binding motifs (i.e., Arg-Gly-Asp sequences) and MMP-sensitive degradation sites from the parent collagen, which inherently support cell adhesion and proliferation.[9] GelMA was synthesized according to a previously published method.[16] For bioink preparation, lyophilized GelMA was dissolved in Dulbecco's phosphate-buffered saline (DPBS; 6% w/v) at 37 °C with 0.3% (w/v) lithium phenyl-2,4,6-trimethylbenzoylphosphinate (Sigma-Aldrich, USA), then stored at 4 °C until further use. A 6% (w/v) gelatin solution was prepared separately by dissolving gelatin powder in DPBS at 37 °C for 30 min and stored at 4 °C. Gelatin can be enzymatically crosslinked using TG, as reported by Ren *et al.*[17] To prepare the TG solution, 20% (w/v) TG was made by dissolving lyophilized TG powder (Moo Glue; Modernist Pantry, USA) in DPBS at 37 °C for 30 min, followed by storage at 4 °C.

To generate a sacrificial template for hollow perfusable channels within the hydrogel matrix, Pluronic F-127 (poloxamer 407), a synthetic biocompatible thermoresponsive hydrogel, was utilized. Its gelation is reversible and temperature-dependent.[18] A 40% (w/v) Pluronic F-127 ink was prepared by dissolving Pluronic F-127 powder (Sigma-Aldrich, USA) in deionized water at 4 °C with continuous stirring for 1 h. The resultant ink was stored at 4 °C until use.

2.2. Perfusable tumor model fabrication

The fabrication of the perfusable 3D hydrogel-based TME model is schematically illustrated in Figure 1. A 3D-printed polylactic acid (PLA) block (15 × 10 × 2 mm^3) was centrally placed in a 35 mm Petri dish. Polydimethylsiloxane (10:1 base-to-curing agent ratio; Sylgard 184, USA) was poured to embed the block and cured at 70 °C overnight. The PLA block was removed, creating a polydimethylsiloxane mold with a central cavity.

A hydrogel mixture comprising 6% (w/v) GelMA and 6% gelatin in a 1:1 ratio was prepared at 37 °C, followed by the addition of TG at a 19:1 hydrogel-to-enzyme ratio. This solution was cast into the polydimethylsiloxane mold to form a thin bottom layer of 1 mm thickness. This layer was cooled at 4 °C to induce rapid gelation. Following this, Pluronic F-127 was printed onto the GelMA–gelatin layer using an extrusion-based 3D bioprinter (TissueStart, Tissuelabs, Switzerland) equipped with a 27G needle. A straight channel (500 μm width) was deposited at a 30 μL/min flow rate. Subsequently, an inkjet-based bioprinting system (PH-47, MicroFab Technologies, USA) was employed to deposit cell-laden GelMA adjacent to the Pluronic channel. The cell-laden droplets (1×10^6 cells/mL) were printed in a single layer with a nominal line spacing of ~100 μm to ensure proximity between the cell-laden region and the channel. Inkjet printing was performed as described in a previous study.[19–21]

After printing, a 1-mm-thick top layer of the GelMA–gelatin mixture was deposited, and the construct was crosslinked under ultraviolet light (10 mW/cm^2, 20 s). The construct was then incubated at 37 °C for 3 h to enable enzymatic crosslinking via TG. To form the perfusable channel, Pluronic F-127 was liquefied at 4 °C and removed with a syringe. A pair of 27G needles was inserted at both ends and connected to a peristaltic pump with a 0.5 mm perfusion tube for medium perfusion. The final tumor model was maintained at 37 °C with continuous medium flow (16 μL/min) for subsequent experiments. This flow rate was selected to generate physiologically relevant shear stress (~0.22 dyn/cm^2), within the reported range for peritoneal organs (0.02–1 dyn/cm^2).[22] In both perfused and non-perfused models, 5 mL of culture medium was used per construct. The medium was refreshed every 48 h during normal culture, and every 24 h during carboplatin treatment to ensure consistent nutrients and drug exposure.

2.3. Shear stress measurement

The wall shear stress (τ) in the perfusion channel was calculated using the following Hagen–Poiseuille equation (**Equation I**) for the 500 μm diameter cylindrical channel[23]:

$$\tau = \frac{4\mu Q}{\pi r^3} \quad \text{(I)}$$

where μ is the dynamic viscosity of the medium, Q is the volumetric flow rate, and r is the channel radius.

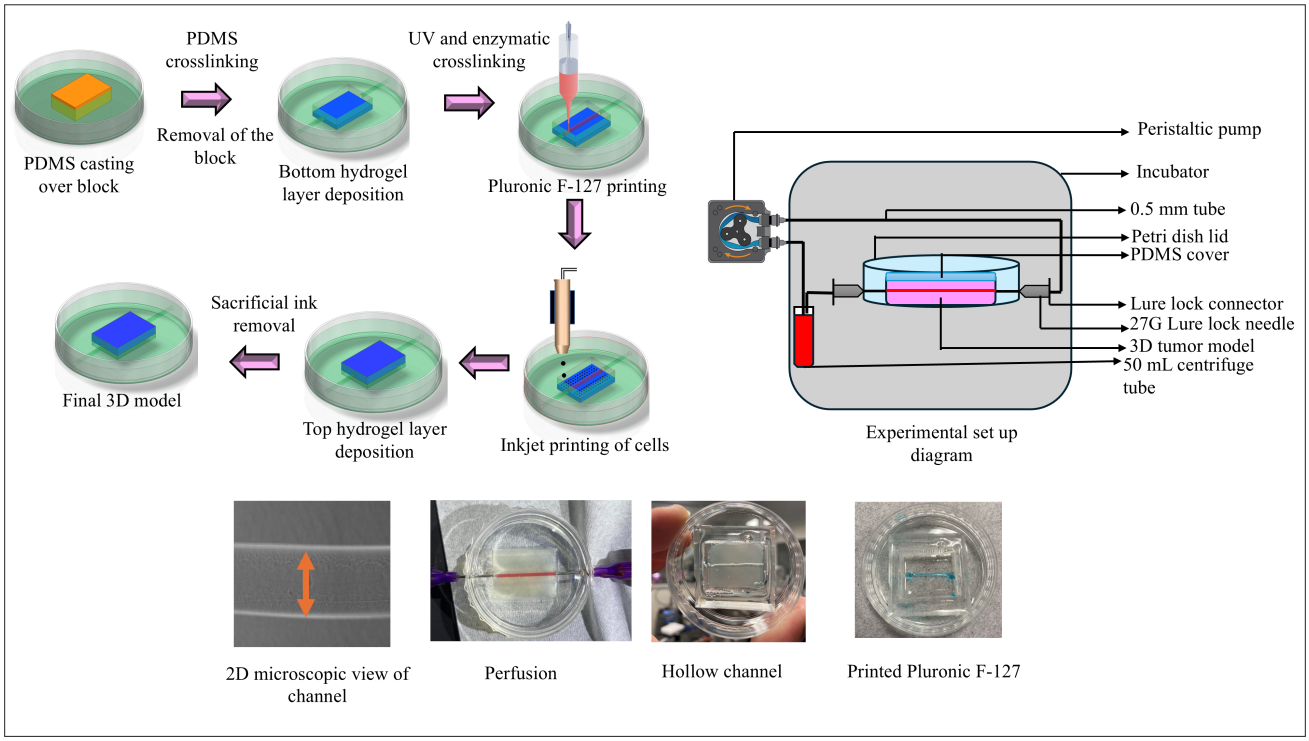

Figure 1. Schematic of the perfusable three-dimensional tumor model fabrication workflow. Abbreviations: 2D, two-dimensional; 3D, three-dimensional; PDMS, polydimethylsiloxane; UV, ultraviolet.

2.4. Hydrogel degradation measurement

Conventional methods have evaluated hydrogel degradation by exposing specimens to collagenase.[24,25] However, monitoring cell-mediated enzymatic breakdown in encapsulated samples provides a more realistic readout of *in situ* remodeling.[26] In this study, enzymatic degradation was evaluated as a percentage mass loss of the hydrogel over 5 days of SKOV3 culture. Immediately after fabrication, cell-laden hydrogels were lyophilized at −50 °C for 12 h, and their initial dry weight (W_0) was recorded. Parallel sets were cultured under perfused and non-perfused conditions and, at Days 1, 3, and 5, were lyophilized under the same conditions to obtain the timepoint dry weight (W_t). The degradation percentage was calculated using **Equation (II):**[26]

$$Degradation(\%) = \left(\frac{W_0 - W_t}{W_0} \right) \times 100 \quad \text{(II)}$$

where W_0 is the dry weight of the specimen immediately after fabrication, and W_t is the dry weight of the specimen after a specific incubation time with SKOV3 cells.

2.5. Cell culture

Human ovarian cancer cell line SKOV3 was purchased from ATCC (United States). Cells were cultured in Dulbecco's Modified Eagle Medium (Sigma-Aldrich, USA), supplemented with 10% fetal bovine serum (Invitrogen, USA) and 1% penicillin–streptomycin (50 U/mL penicillin, 50 µg/mL streptomycin; Invitrogen, USA) at 37 °C and 5% carbon dioxide. Before bioprinting, cells were detached using 0.25% trypsin-ethylenediaminetetraacetic acid (Corning, USA), centrifuged, and resuspended in 6% (w/v) GelMA at 1×10^6 cells/mL for bioink preparation.

2.6. Cell morphology, migration, proliferation, and viability analysis

Cell morphology was quantified using aspect ratio and circularity, extracted from live-cell images via ImageJ (version 2.14.0). A high aspect ratio indicates an elongated, spindle-like shape associated with increased motility and epithelial-to-mesenchymal transition. In contrast, low values and high circularity reflect rounded, less migratory, or apoptotic phenotypes.[27,28] Morphology was assessed using fluorescence microscopy (AMF4300, EVOS FL, USA). Constructs were perfused with DPBS, fixed with 4% formaldehyde, and permeabilized using Triton X-100. Staining was performed with phalloidin (F-actin, green;

Santa Cruz Biotechnology Inc., USA) and 4',6-diamidino-2-phenylindole (nuclei, blue; Santa Cruz Biotechnology Inc., USA), followed by incubation in the dark at room temperature for imaging.

To assess cell migration, live-cell fluorescence images were acquired at 2-h intervals over 3 days. The displacement of individual cell nuclei was tracked relative to their initial positions at time zero. Migration speed was determined by calculating the total distance traveled by each nucleus and dividing it by the corresponding time interval. The global turning angle was used to evaluate directional changes in cell migration trajectories. The normalized cell proliferation index was calculated by dividing the total cell count on Day 7 by the initial seeding density within the tumor construct. A standard live/dead assay was used to assess cell viability, as previously reported.[29] Cell viability was quantified as the percentage of live cells relative to the total number of cells in each sample.

2.7. Scanning electron microscopy imaging of the hydrogel

To evaluate the microstructure of the hydrogels before and after experimentation, the samples were perfused with DPBS for 3 h to remove residual culture medium and cellular waste. Subsequently, the hydrogels were frozen at −80 °C overnight and lyophilized using a freeze dryer (Labconco, USA) for 3 days. Prior to the scanning electron microscopy (SEM) imaging, the dried samples were gold-coated using a sputter coater (Ted Pella Inc., USA) at 0.1 mA/mbar for 30 s at room temperature. The microstructures were then imaged using a scanning electron microscope (Phenom Pharos, Thermo Fisher Scientific, USA), and the images were analyzed using the ImageJ software.[28]

2.8. Experimental design and data analysis

In both perfused and non-perfused models, a central hollow channel was embedded during fabrication to ensure consistency in spatial geometry and to enable direct comparisons between groups. While only the perfused model received continuous medium flow through this channel, the non-perfused model retained the same channel structure for distance mapping and spatial sampling, but no dynamic perfusion was applied. To evaluate the influence of perfusion and spatial proximity to the perfusion channel on cellular behavior, the tumor constructs were segmented into three distinct regions based on radial distance from the channel: 0–300, 300–600, and 600–900 μm. These zones were selected based on the known diffusion limit of oxygen (~200 μm) and prior studies showing reduced viability beyond 500–600 μm, with 900 μm representing an extreme diffusion-limited condition.[30,31] The 0–300 μm zone was expected to represent a well-perfused region with optimal access to nutrients and oxygen, thereby supporting higher viability, proliferation, and motility. In contrast, the 600–900 μm zone was expected to model diffusion-limited, quasi-anoxic regions, leading to suppressed cellular activity and survival, closely mimicking necrotic tumor cores. The flow rate of 16 μL/min was chosen to achieve low interstitial shear stress (~0.22 dyn/cm^2), within the physiological range observed in tumors, and was expected to induce mechanotransductive responses that enhance cellular elongation and directional migration.[22] Cells were cultured in the tumor model for 7 days, where Day 1 was the initial day of cell encapsulation and Day 7 was the final day of cell culture. Cell morphology, proliferation, and viability were measured on Day 1 and Day 7 of these experiments. To assess cell migration, SKOV3 cells were cultured for 4 days to enable matrix degradation, remodeling, and tumor-like tissue establishment. Migration speed was then quantified over the subsequent 3 days, with the first day of tracking designated as Day 1 and the final day as Day 3. Quantitative parameters from cells within each region were extracted using the ImageJ software, based on live-cell fluorescence images acquired at 2-h intervals. To evaluate the effect of the chemotherapeutic drug, following an initial 4-day culture period enabling cellular adaptation and tumor establishment, carboplatin with varying concentrations (0–30 μM) was introduced into the perfusion channel and maintained for 3 consecutive days. This concentration range was chosen to investigate the dose-dependent suppression of cellular response. For consistency, the day of initial drug introduction was designated as Day 1, and the final day of perfusion as Day 3. All analyses were focused on the perivascular region of the tumor model, specifically the area located 0–300 μm from the perfusion channel, where nutrient and drug diffusion are presumed to be most effective. All experiments were independently repeated at least three times under identical conditions. Statistical analysis was performed using the analysis of variance and Tukey's post hoc test (Python, version 3.11), and differences were considered statistically significant at $p < 0.05$.

3. Results

3.1. Effect of perfusion and spatial gradients on cell behavior

3.1.1. Effect on cell morphology

To evaluate the impact of perfusion on cell morphology, aspect ratio and circularity were quantified from bright-field images of SKOV3 cells after 7 days of culture under perfused and non-perfused conditions at distances of 300, 600, and 900 μm from the channel (Figure 2A). In the perfused model, the aspect ratio significantly ($p < 0.05$) decreased (3.50–2.65) and circularity increased

(0.23–0.34) with distance, indicating reduced elongation. In the non-perfused model, the lack of convective flow eliminated nutrient/oxygen gradients, resulting in uniform hypoxia and metabolic stress across all regions. This led to statistically insignificant morphological changes (aspect ratio 1.98–2.02, circularity 0.39–0.41, $p > 0.05$), with slight variations attributed to stochastic cellular responses rather than mechanistic differences. Qualitative observation of cell morphology supports these quantitative findings (Figure 2B). On Day 1, both models showed similar cell shapes; by Day 7, the perfused model developed a polarized, spindle-like morphology typical of invasive phenotypes, while the non-perfused model retained rounded forms. These images illustrate the development of a polarized cell morphology over time in perfused 3D tumors, versus the retention of a rounded morphology in non-perfused tumors.

Fluid shear stress from perfused media is a key regulator of cell morphology in 3D tumor models. Even low interstitial shear levels provide mechanical cues that influence cell behavior via mechanoreceptors. Prior studies have shown that shear exposure enhances cell spreading and reduces circularity, indicating a transition to a motile, polarized phenotype.[32] In our model, cells near the perfusion channel were exposed to higher shear, which exhibited elongated morphologies with higher aspect ratios. This spatial variation also reflects differences in nutrient and oxygen availability; cells proximal to the channel were well-nourished, while those farther away faced diffusion limitations and metabolic waste accumulation.[33] In non-perfused conditions, the absence of convective flow led to disorganized actin structures, reduced focal adhesions, and spherical cell shapes due to stress-induced adaptation.[34] These findings underscore the role of perfusion in maintaining physiological morphology and preventing stress-driven rounding in 3D tumor environments.

3.1.2. Effect on cell migration

Figure 3A presents the average migration speed of SKOV3 cells over 3 days in both perfused and non-perfused 3D tumor models. In the perfused condition, average cell migration speed decreased significantly with increasing distance from the channel: 28.98 μm/day at 0–300 μm, 26.57 μm/day at 300–600 μm, and 21.27 μm/day at 600–900 μm ($p < 0.05$). In contrast, cells in the non-perfused model exhibited consistently lower migration speeds, ranging from 13.05 to 13.57 μm/day and 13.57–12.71 μm/day across the same spatial zones. The representative bright field images demonstrate typical 3-day single cell migration in the 0–300 μm region in both models (Figure 3B). Figure 3C and D illustrates representative migration trajectories and angular orientation plots of cells in both conditions. In the perfused model, with increasing distance from the perfusion channel (0–300, 300–600, 600–900 μm), the 3-day mean net displacement decreased significantly from 82.5 to 58.5 μm and from 58.5 to 39.1 μm ($p < 0.05$). Furthermore, cells in the 0–300

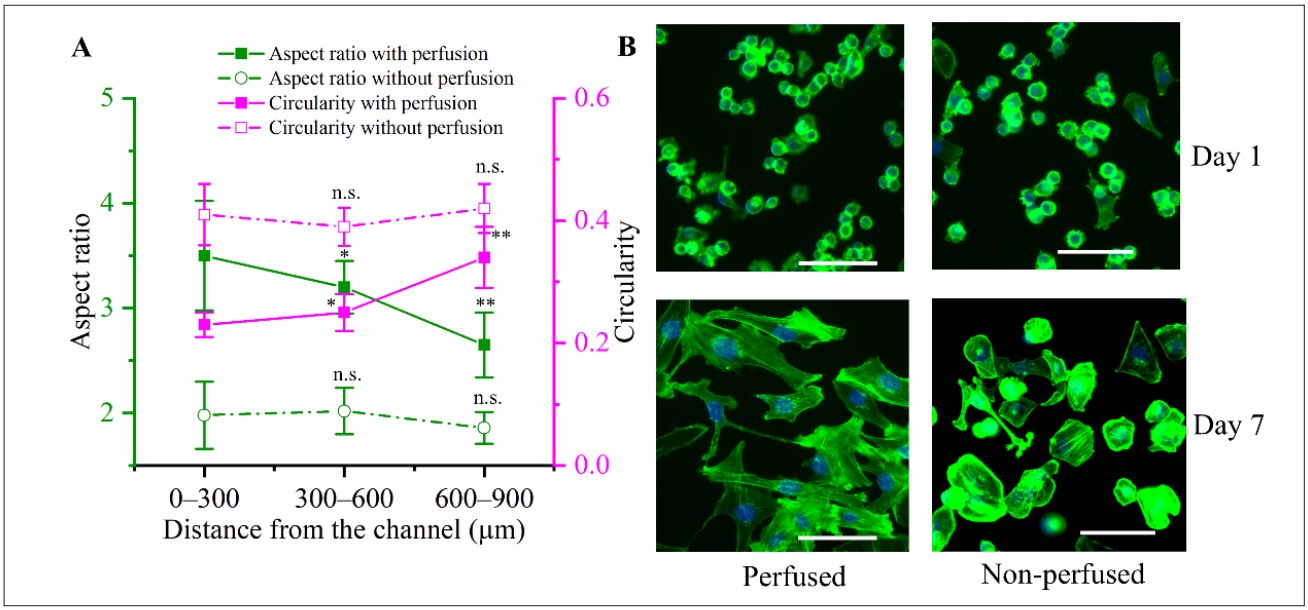

Figure 2. Effect of perfusion on cellular morphology. (A) Comparison of cellular aspect ratio and circularity of SKOV3 cells at Day 7, depending on the distance from the perfusion channel, grown in perfused and non-perfused conditions. (B) Representative fluorescence images of cell morphology at Day 1 and Day 7 within the 0–300 μm region in both models. Green fluorescence shows cytoskeletal staining of F-actin with phalloidin, and blue fluorescence shows nuclear counterstain. Scale bar: 100 μm; magnification: 40×. Notes: $n = 3$, n.s. = not significant, $^{*}p < 0.05$, $^{**}p < 0.01$, $^{***}p < 0.001$.

μm region displayed directed movement aligned with or toward the flow direction of the medium. However, as the distance increased, cell trajectories became progressively more random. Quantitative analysis showed that 63% of cells within 0–300 μm oriented along the flow direction, decreasing to 45% in the 300–600 μm zone and 40% in the 600–900 μm region ($p < 0.05$). In the non-perfused model, migration paths remained random across all regions. This spatial trend suggests that interstitial flow provides directional cues that guide cell orientation near the perfusion channel.

Oxygen gradients can serve as directional cues for cancer cell migration. In hydrogel systems, sarcoma cells have been shown to move toward more oxygenated regions, mimicking vessel-directed migration.[35] In our model, cells within ~300 μm of the perfusion channel had sufficient

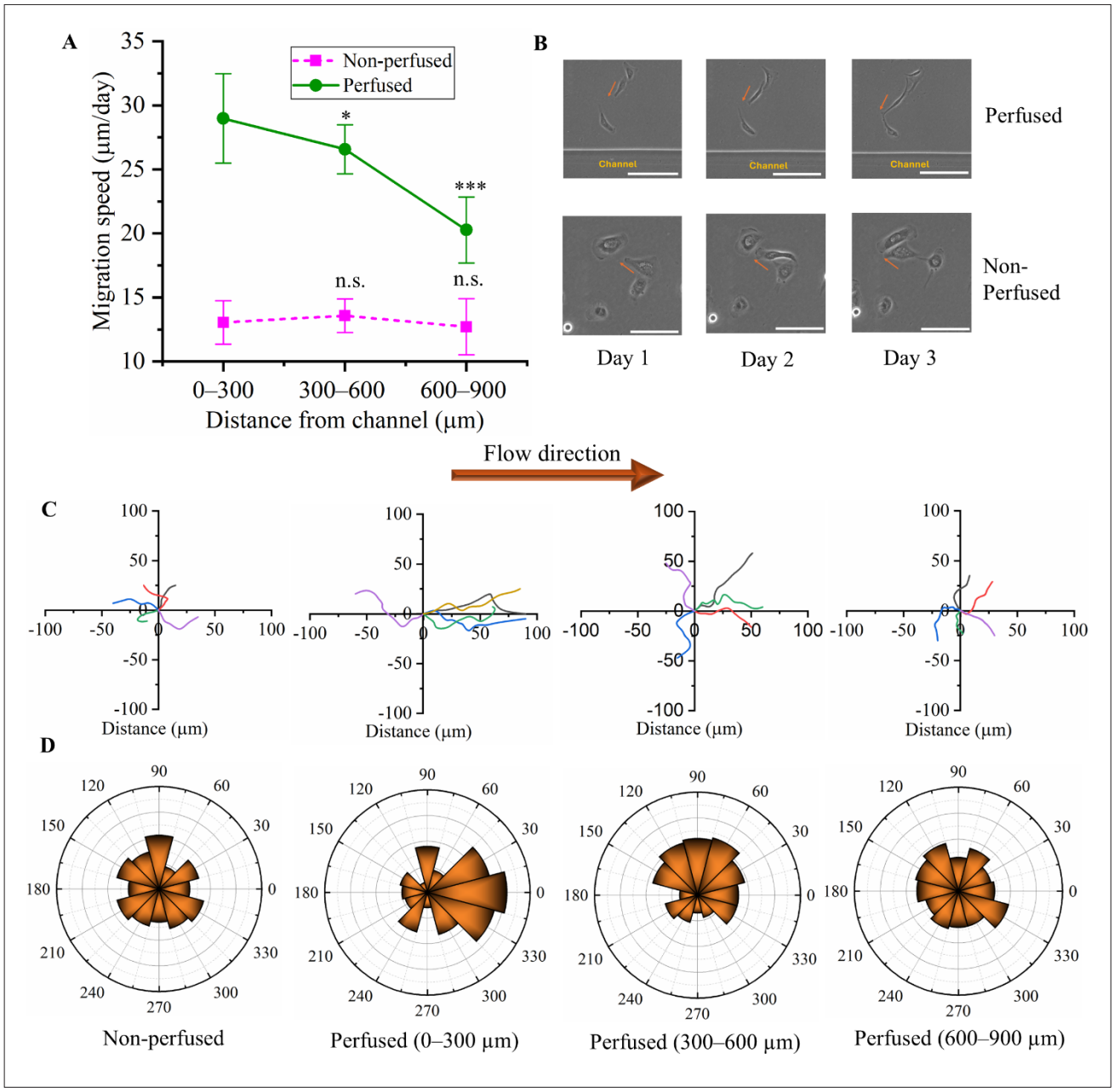

Figure 3. Effect of perfusion on cell migration. (A) Effect of perfusion on cell migration speed. (B) A typical cell migration representation from Day 1 to Day 3 within the 0–300 μm region in the perfused and non-perfused model (arrow indicates cell migration trajectory). Scale bar: 100 μm; magnification: 40×. (C) Representative typical cell migration trajectories. (D) Angular orientation distributions as a function of distance from the perfusion channel under perfused and non-perfused culture conditions. Notes: $n = 3$, n.s. = not significant, $^{*}p < 0.05$, $^{**}p < 0.01$, $^{***}p < 0.001$.

oxygen to support migration and may have sensed and followed the gradient. Cells further from the channel had reduced oxygen and nutrients, which impaired motility. Additionally, interstitial flow near the channel provides mechanotactic signals and fluid shear that guide migration by creating intracellular tension gradients. This has been linked to β1-integrin and focal adhesion kinase polarization, promoting protrusion along the flow direction.[36] Similarly, OVCAR-3 cells exposed to moderate shear stress showed elongated morphologies and aligned migration.[37] Thus, in our perfused model, combined oxygen availability and fluid-induced mechanical cues near the perfusion channel likely promoted directional migration, underscoring the importance of perfusion gradients in regulating tumor cell motility.

3.1.3. Effect on cell proliferation

Figure 4A illustrates the cell proliferation index as a function of distance from the perfused channel after 7 days, comparing conditions with and without perfusion. The data reveal a decline in the proliferation index with increasing distance from the channel under perfused conditions, decreasing from 3.8 at 0–300 μm to 3.2 at 300–600 μm, and further to 2.9 at 600–900 μm. In contrast, under non-perfused conditions, the overall proliferation index was significantly lower ($p < 0.05$) and showed minimal variation with distance. Specifically, the proliferation indices across the same regions were 2.1, 2.3, and 2.0, respectively. The representative bright field images demonstrated a substantial increase in cell density over time in the perfused model, highlighting the positive effect of continuous medium flow on cell growth (Figure 4B). In contrast, the non-perfused model exhibited minimal changes in cell density, underscoring the critical role of perfusion in supporting cell proliferation within the GelMA–gelatin tumor model.

In the 3D tumor model, the perfusion channel mimics a blood vessel, continuously delivering oxygen and nutrients to support cell metabolism and proliferation. Cells near the channel benefit from normoxic conditions and show enhanced growth, as observed by Gilmore *et al.*[38] in perfused 3D breast tumor models. However, increasing distance from the channel leads to diffusion-limited gradients of oxygen and glucose, resulting in hypoxia and reduced proliferation.[39] While perfusion improves nutrient delivery via convection, spatial limitations persist, making proximity to the channel a key determinant of cellular behavior.[40] In non-perfused models, uniform hypoxia and accumulation of metabolic waste, such as lactic acid and carbon dioxide, create an acidic environment that induces cell cycle arrest and inhibits proliferation.[41]

3.1.4. Effect on cell viability

Figure 5A illustrates the cell viability percentages in perfused and non-perfused tumor models after 7 days of culture, as a function of distance from the perfusion channel. In the perfused tumor model, cell viability progressively decreased with increasing distance from the perfusion channel, from 96% at 0–300 μm to 93% at 300–600 μm and

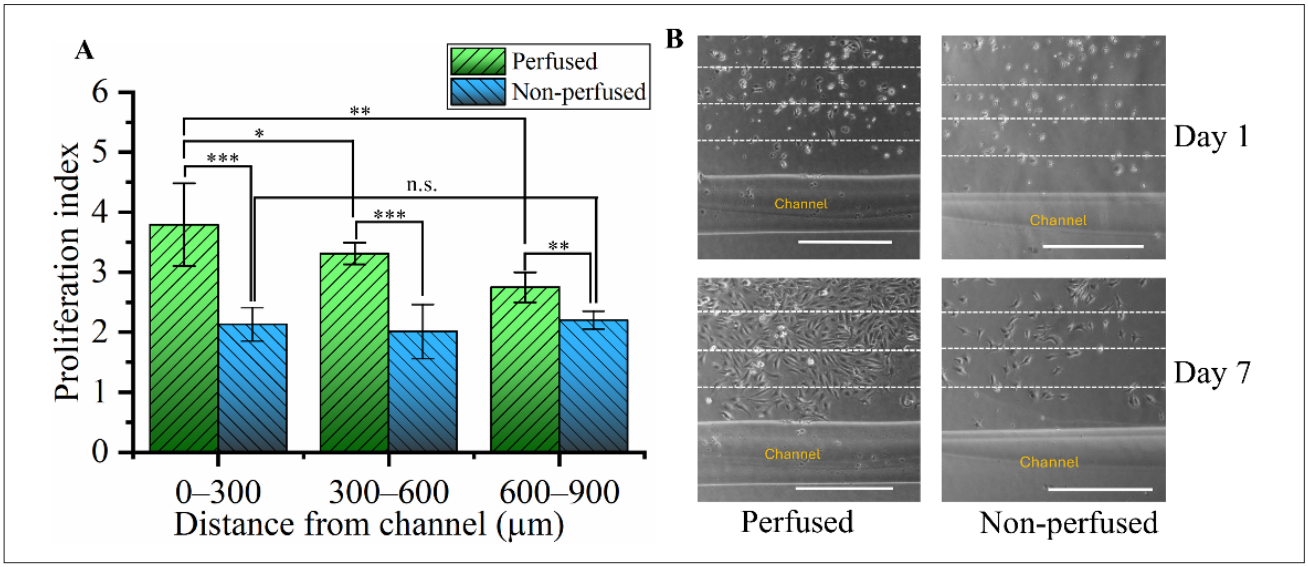

Figure 4. Effect of perfusion on cell proliferation. (A) Comparison of cell proliferation index as a function of distance from the perfusion channel. (B) Representative bright field images at Day 1 and Day 7 under perfused and non-perfused culture conditions. White dashed lines show three regions (0–300, 300–600, and 300–600 μm) adjacent to the channel. Scale bar: 1000 μm; magnification: 4×. Notes: $n = 3$, n.s. = not significant, $^{*}p < 0.05$, $^{**}p < 0.01$, $^{***}p < 0.001$.

88% at 600–900 μm. In contrast, the cell viability in the non-perfused tumor model remained significantly lower, ranging from 69% to 71% across all distances measured ($p < 0.05$). Qualitative observation of cell viability supports these quantitative findings (Figure 5B).

In perfused 3D tumor models, cells near the channel receive sufficient oxygen and nutrients, supporting high viability. However, as the distance increases, reliance on diffusion becomes inadequate beyond ~200 μm, leading to hypoxia and reduced survival.[42] Perfusion also facilitates waste removal, but in distal regions, limited diffusion causes accumulation of carbon dioxide and lactate, further compromising cell viability. In contrast, non-perfused models lack convective flow, resulting in widespread nutrient depletion and toxic buildup. By culturing HCT-116 colon carcinoma cells around a perfused microfluidic lumen, Ayuso *et al.*[43] observed minimal cell death near perfused lumens, with necrosis increasing toward the construct core. Similarly, using a breast cancer microfluidic model, Pasini *et al.*[40] reported uniform viability under perfusion, while non-perfused systems showed extensive nutrient-starved zones. These findings highlight that distance-dependent gradients in oxygen and metabolites are major drivers of cell loss in 3D models, and perfusion is essential for sustaining viability, particularly in deeper tissue regions where diffusion alone is insufficient.

3.2. Effect of perfusion of carboplatin on cell behavior

In this section, we examined the effect of the chemotherapeutic agent carboplatin on the behavior of SKOV3 ovarian cancer cells within a perfused 3D tumor model. Following an initial 4-day culture period to allow cellular adaptation and tumor establishment, carboplatin was introduced into the perfusion channel at varying concentrations and maintained for 3 consecutive days. Cellular responses, including morphology, migration, proliferation, and viability, were assessed during this drug exposure period. For consistency, the day of initial drug introduction was designated as Day 1, and the final day of perfusion as Day 3. All analyses were focused on the perivascular region of the tumor model, specifically the area located 0–300 μm from the perfusion channel, where nutrient and drug diffusion are presumed to be most effective.

3.2.1. Effect on cell morphology

Figure 6A illustrates the effect of increasing carboplatin concentration on cellular morphology after 3 days of drug exposure. As the drug concentration increased from 0 to 10, 20, and 30 μM, a marked decrease in cellular aspect ratio was observed, from 3.15 to 2.88, 2.20, and 1.17, respectively ($p < 0.05$). Concurrently, cell circularity increased from 0.25 to 0.31, 0.43, and 0.70. Representative images of cell morphology confirm that SKOV3 cells initially exhibited an elongated shape in the absence of the drug (Figure 6B). Following exposure to increasing concentrations of carboplatin, cells progressively adopted a more rounded morphology by Day 3, indicative of cytoskeletal remodeling and loss of polarity. In the control group (0 μM), such morphological changes were not observed, consistent with the absence of drug exposure.

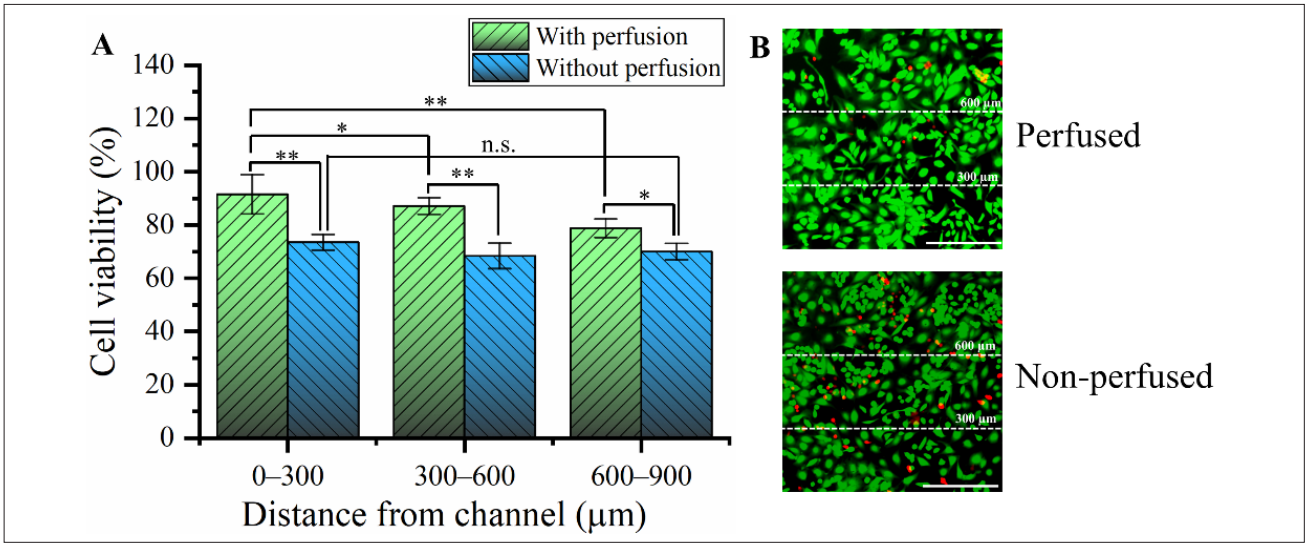

Figure 5. Effect of perfusion on cell viability. (A) Comparison of cell viability as a function of the distance from the perfusion channel. (B) Representative cell viability in perfused and non-perfused conditions after 7 days of cell culture. White dashed lines showing three regions (0–300, 300–600, 300–600 μm) adjacent to the channel, green and red fluorescence show the live and dead cells, respectively. Scale bar: 400 μm; magnification: 10×. Notes: $n = 3$, n.s. = not significant, $^{*}p < 0.05$, $^{**}p < 0.01$, $^{***}p < 0.001$.

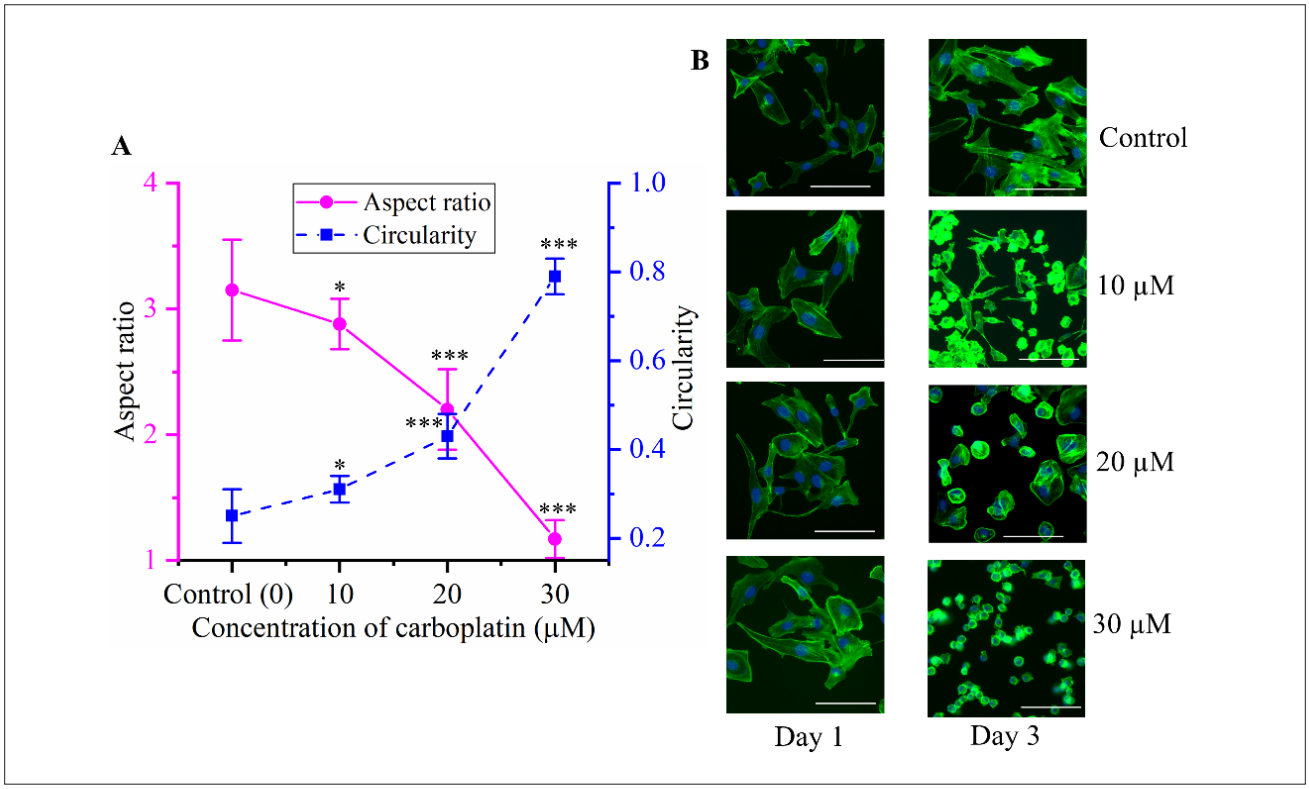

Figure 6. Effect of carboplatin on cellular morphology. (A) Effect of carboplatin drug concentration on cellular morphology after 7 days of cell culture. (B) Representative of cell morphology with an increase in concentration of drug on Day 1 and Day 3 within the 0–300 μm region in the perfused model. Green fluorescence shows cytoskeletal staining of F-actin with phalloidin, and blue fluorescence shows nuclear counterstain. Scale bar: 100 μm; magnification: 40×. Notes: $n = 3$, $^{*}p < 0.05$, $^{**}p < 0.01$, $^{***}p < 0.001$.

Carboplatin, like other platinum-based chemotherapeutics, induces extensive DNA crosslinking that activates the DNA damage response. This typically forces cells into cell-cycle arrest and triggers apoptosis.[44] One key reason for the rounding of cells under carboplatin is the cytoskeleton disruption and loss of cell structural integrity during drug-induced stress. Prior studies showed that chemotherapeutic agents altered the organization of actin filaments and microtubules, leading to changes in cancer cell stiffness, shape, and attachment.[45] In our experiment, the decreased aspect ratio with higher carboplatin doses reflects such depolymerization of F-actin stress fibers and alterations in microtubule networks. Furthermore, early-stage apoptosis involves the disassembly of focal adhesions and detachment from the matrix, coinciding with cells turning from an elongated, spread morphology to a contracted, round shape.[46] Thus, the observed increase in cellular circularity with rising carboplatin concentration in our experiment reflects apoptosis-associated morphological changes and reduced cell–matrix adhesion.

3.2.2. Effect on cell migration

Figure 7A illustrates the quantitative effect of increasing carboplatin concentrations on SKOV3 cell migration speed and visual representations of individual cell movement. As the drug concentration increased from 0 to 10, 20, and 30 μM, the average migration speed significantly declined from 28.98 to 23.12, 12.42, and 4.68 μm/day, respectively ($p < 0.05$). Figure 7B presents representative migration trajectories and angular orientation plots of cells under varying drug exposures. In the control group (0 μM), cells exhibited elongated morphology with a polarized cytoskeleton, enabling persistent and directed migration toward the perfusion channel, largely following the medium flow direction. In contrast, cells exposed to higher carboplatin concentrations lost their polarized morphology, adopted a rounded, amoeboid shape, and exhibited random, non-directional movement. The average net displacement over 3 days significantly decreased from 82.5–30.9 to 22.3–14.5 μm with an increase in drug concentration from 0 to 30 μM ($p < 0.05$). Moreover, quantitative analysis revealed that approximately 63%

of cells in the control condition aligned with the flow direction, which was significantly reduced to 41% at 30 μM carboplatin ($p < 0.05$). These findings suggest that carboplatin disrupts cytoskeletal organization and impairs the ability of cancer cells to sense and respond to directional cues, thereby inhibiting directed migration.

A primary reason for the slowed migration with the increase in drug concentration is the cytotoxic action of carboplatin on the cancer cells. In HN-3 carcinoma cells, carboplatin triggered an accumulation of reactive oxygen species that promoted apoptosis, correlating with a marked suppression of migration *in vitro*.[47] Beyond outright cell death, sublethal exposure to carboplatin can disrupt the cellular machinery of migration. Studies showed that carboplatin exposure led to lower expression of MMP2 and MMP9 in lung cancer cells, two MMPs crucial for degrading the ECM during cell invasion.[48] This reduction in MMP2/9 suggests that carboplatin not only physically slows cells by harming them but also diminishes their invasive machinery at the molecular level, reinforcing the decrease in migratory capacity. Furthermore, in our control condition, SKOV3 cells clearly adopted a polarized,

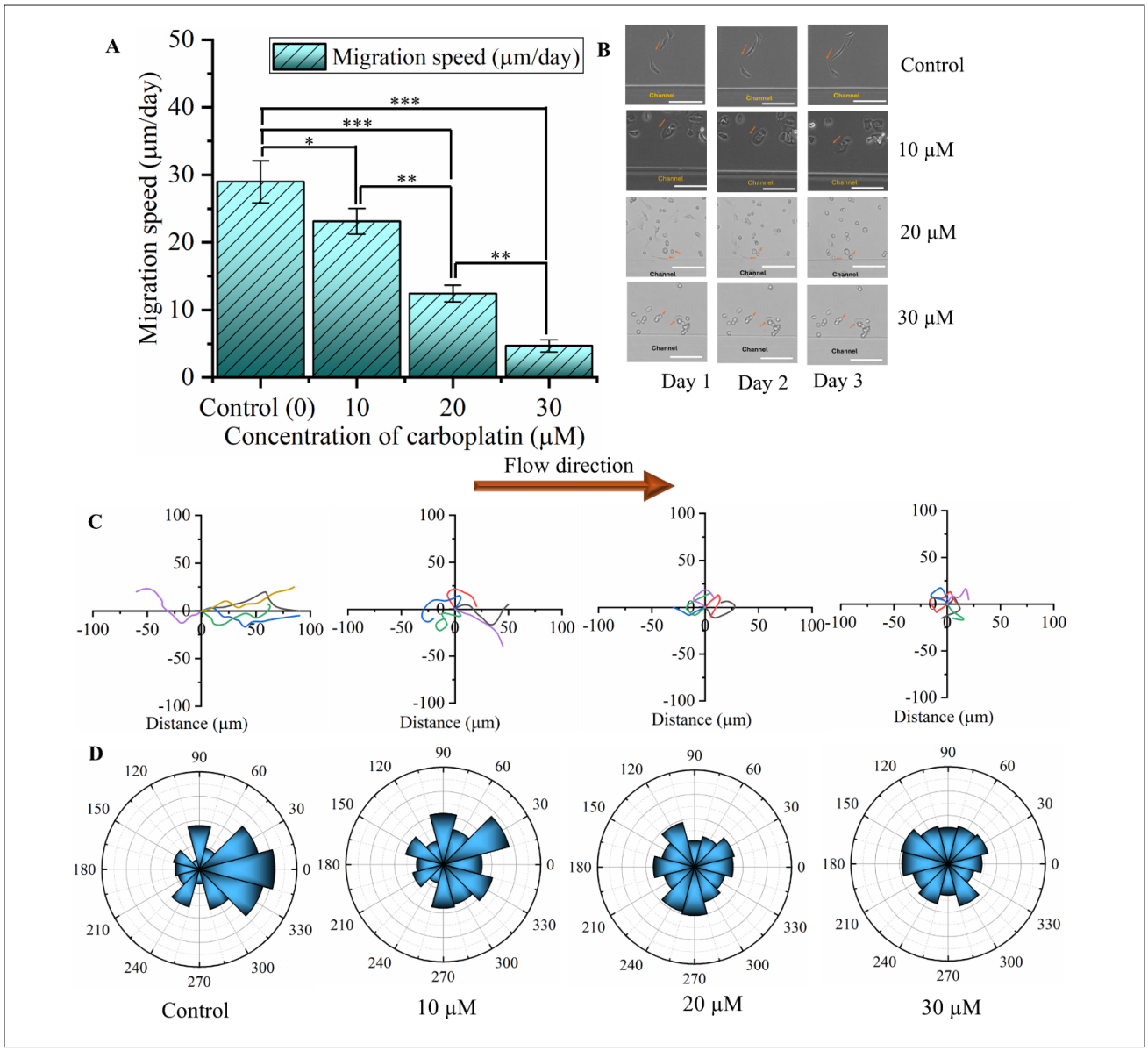

Figure 7. Effect of carboplatin on cell migration. (A) Effect of carboplatin concentration on SKOV3 cell migration speed. (B) A typical cell migration representation from Day 1 to Day 3 within the 0–300 μm region. Scale bar: 100 μm; magnification: 40×. (C) Representative migration trajectories. (D) Angular orientation distributions within the 0–300 μm region as a function of different carboplatin concentrations. Notes: $n = 3$, $^{*}p < 0.05$, $^{**}p < 0.01$, $^{***}p < 0.001$.

mesenchymal-like shape, enabling them to move *en masse* toward the channel. However, carboplatin-treated cells could no longer maintain a polarized cytoskeleton. The high drug concentrations likely cause actin cytoskeleton disassembly and loss of focal adhesions, resulting in cells that round up and lose their front-back orientation. Consistent with our observations, the literature reports that non-polarized cells extend multiple small protrusions and barely move in any one direction.[49] This mirrors the random migration observed under carboplatin: cells protrude and retract in different directions without sustained movement, leading to a random walk rather than a persistent path. Specifically, our high-dose observations (30 μM) showed many cells in a nearly ameboid, round state, unable to form stable lamellipodia, resulting in a loss of persistent, directional migration. Another intriguing aspect of our results is the interplay between fluid flow cues and drug effects. In the control condition, cells migrated toward the perfused channel, aligning their trajectories with the medium flow direction. This suggests that flow-mediated guidance was at work in our tumor model. Prior studies have shown that cancer cells frequently respond to interstitial fluid flow by migrating toward fluid movement.[50] Carboplatin treatment, however, disrupted this directed migration, likely by impairing the molecular pathways responsible for flow sensing and directional guidance.[51]

3.2.3. Effect on cell proliferation

Figure 8A shows the dose-dependent suppression of cancer cell proliferation over 3 days. In the control (0 μM carboplatin), SKOV3 ovarian carcinoma cells proliferated robustly over 3 days (proliferation index 2.3), indicating more than a twofold increase in cell population. However, with increasing carboplatin concentration, the net cell growth significantly ($p < 0.05$) declined: 10 μM yielded a lower proliferation index of 1.85, 20 μM was near-growth arrest (1.1), and at 30 μM the index dropped to 0.46, indicating the cell count after treatment was less than the initial seeding (net cell loss). Qualitative observation of cell proliferation supports these quantitative findings (Figure 8B).

This inverse relationship between drug dose and proliferation is consistent with extensive evidence that higher carboplatin doses induce greater cytotoxicity in cancer cells.[52] The reduction in proliferation index with higher carboplatin concentrations can be explained by the drug's well-characterized mechanisms of action.

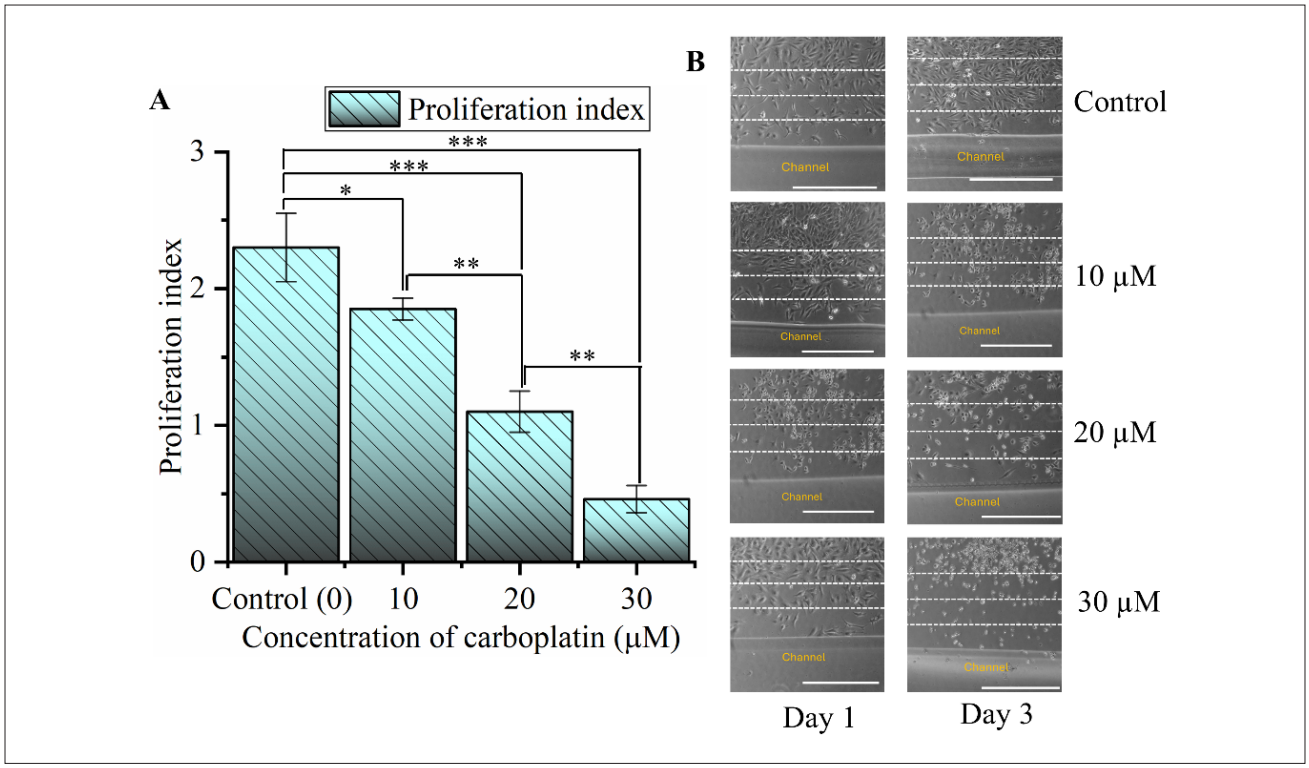

Figure 8. Effect of carboplatin on cell proliferation. (A) Effect of carboplatin concentration on SKOV3 cell proliferation index. (B) Representative bright field images of cell proliferation for 3 days of carboplatin exposure. White dashed lines showing three regions (0–300, 300–600, and 300–600 μm) adjacent to the channel. Scale bar: 1000 μm; magnification: 4×. Notes: $n = 3$, $^{*}p < 0.05$, $^{**}p < 0.01$, $^{***}p < 0.001$.

Carboplatin covalently binds DNA, forming intra- and interstrand DNA crosslinks, and bulky adducts, causing cell cycle arrest. The arrest allows time for DNA repair, but if the damage is too severe or irreparable, cells undergo programmed cell death (apoptosis).[44] At lower drug doses, some cancer cells may manage to repair sub-lethal DNA damage or enter temporary cell-cycle arrest. Hence, a fraction of cells continue dividing; this explains why we still observed modest net growth at 10–20 μM. In contrast, higher doses like 30 μM produce a greater accumulation of DNA adducts and overwhelming DNA damage.[52] Consequently, a large portion of the cell population either remains permanently growth-arrested or undergoes apoptosis. The proliferation index <1 at 30 μM reflects this outcome: cell death and permanent cell-cycle exit outpace any residual cell divisions, leading to a net decrease in viable cell number.

3.2.4. Effect on cell viability

In this section, we investigated the differential response of SKOV3 cells to different concentrations (0–50 μM) of carboplatin exposure using our 3D perfused tumor model. Figure 9A demonstrates how carboplatin affected cell viability. SKOV3 cells showed a classic dose-dependent cytotoxic response: viability dropped from 95% (no drug) to 82% at 10 μM, 65% at 20 μM, 41% at 30 μM, and down to only 5% at 50 μM. Increasing carboplatin exposure caused a statistically significant ($p < 0.05$) loss of viable cells in the sensitive population. This trend is consistent with typical carboplatin sensitivity ranges reported for ovarian cancer lines. It was reported that SKOV3 cells had a carboplatin half-maximal inhibitory concentration of around 12.4 μM,[53] indicating that doses above 20 μM overwhelm their ability to survive. Qualitative observation of cell viability supports these quantitative findings (Figure 9B).

The primary mechanism of carboplatin involves direct damage to cellular DNA.[54] The sharp decline in viability we observed for the SKOV3 cells with rising carboplatin dose is a direct consequence of this mechanism: as more platinum DNA adducts accumulate, a larger fraction of cells undergo irreversible cell-cycle arrest, lethal DNA damage, and apoptosis.[54] *In vitro* studies consistently showed that escalating carboplatin concentrations caused a dose-dependent decline in cancer cell viability, even in 3D tumor models. Ovarian cancer spheroids exposed to increasing carboplatin doses exhibited progressively lower viable cell fractions compared to untreated controls.[55] Notably, in SKOV3 ovarian cancer cells, carboplatin monotherapy significantly suppressed cell growth in a concentration-dependent manner, confirming that viability drops as the dose rises.

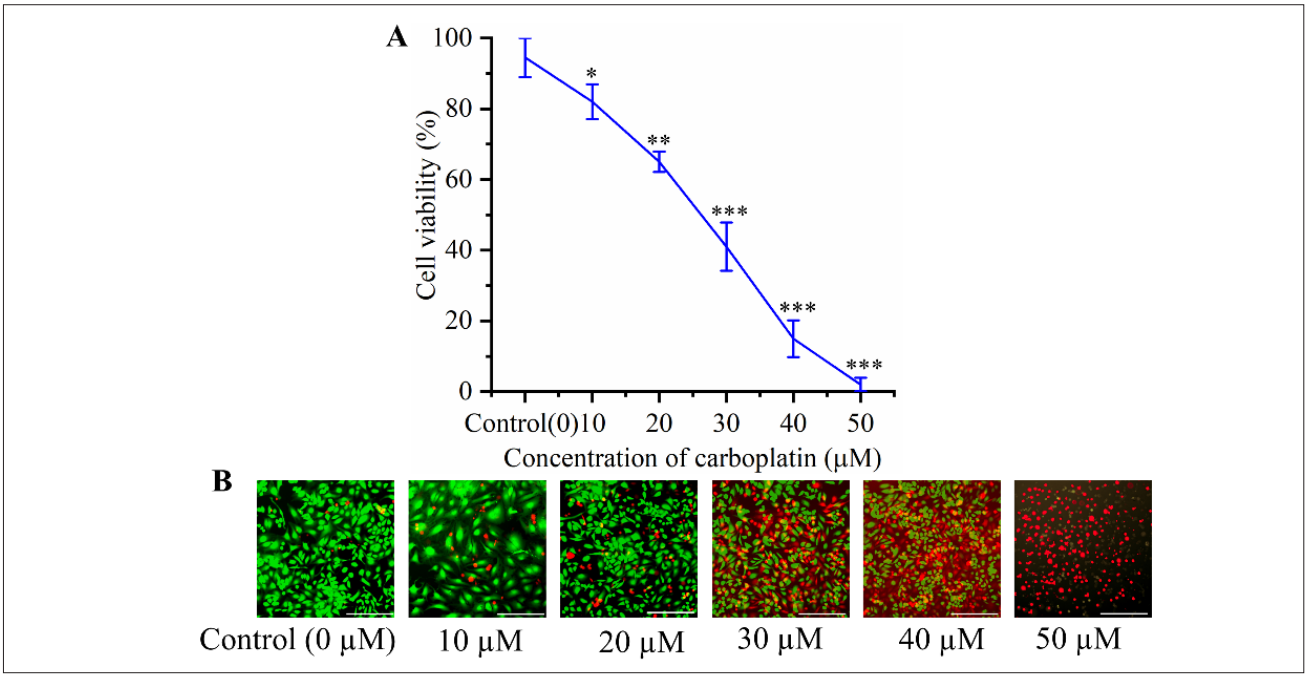

Figure 9. Effect of carboplatin on cell viability. (A) Effect of carboplatin concentrations on SKOV3 cell viability. (B) Representative cell viability after 3 days of carboplatin exposure within the 0–300 μm region. Green and red fluorescence show the live and dead cells, respectively. Scale bar: 400 μm; magnification: 10×. Notes: $n = 3$, $^{*}p < 0.05$, $^{**}p < 0.01$, $^{***}p < 0.001$.

4. Discussion

In this study, we developed a perfusable 3D tumor model with SKOV3 ovarian cancer cells to investigate the effects of spatial gradients and chemotherapeutic exposure on cell behavior. A central hollow channel enabled continuous medium flow, generating nutrient and oxygen gradients across the construct. Prior studies have demonstrated that perfusable channels significantly enhance mass transport in 3D hydrogels. Lieberthal *et al.*[56] perfused red dye and fluorescent tracers through a 3D-printed liver hydrogel and observed rapid radial diffusion into the surrounding matrix.[56] Similar diffusion-enhancing effects of perfusable microchannels have been shown using dye penetration in engineered scaffolds and vascular-like synthetic microfluidic, supporting our zone-based interpretation of spatial gradients in cell behavior.[57,58] Cells within 0–300 μm of the channel accessed abundant oxygen and nutrients, supporting high viability, metabolism, and proliferation. In contrast, cells at 600–900 μm relied on diffusion alone, leading to hypoxia and nutrient deprivation, conditions known to impair cell function beyond ~200 μm in hydrogels.[59] These gradients significantly influenced cellular responses: cells near the channel exhibited an elongated, spindle-like morphology and higher motility, consistent with an active, mesenchymal phenotype. This behavior is driven by improved metabolic conditions and cytoskeletal remodeling. Additionally, shear stress from the interstitial flow near the channel may serve as a mechanical cue, further enhancing cell elongation and directed migration. These findings highlight how perfusion critically shapes tumor cell behavior in 3D environments.

Gelatin methacrylate hydrogels are designed to mimic the ECM and can be enzymatically degraded by cells. GelMA and gelatin contain peptide motifs (derived from collagen) that are cleavable by MMPs.[60] When cells are embedded in the matrix, they secrete MMPs and other proteases that break down the surrounding hydrogel network. Figure 10 quantifies the hydrogel degradation rate by SKOV3 cells over 5 days of cell culture in perfused versus non-perfused conditions. Under continuous perfusion, 6% GelMA–gelatin hydrogel degraded from 9.39% (Day 1) to 26.87% (Day 3) and 68.0% (Day 5), with each interval showing a significant increase ($p < 0.05$). By contrast, static (non-perfused) constructs showed substantially lower degradation, rising from 2.50% (Day 1) to 11.8% (Day 3) and 31.5% (Day 5). At each time point, perfused samples exhibited greater mass loss than non-perfused counterparts ($p < 0.05$), indicating accelerated matrix degradation and remodeling under flow. Furthermore, this cell-mediated degradation effectively enlarges void spaces or "pores" within the hydrogel.[61] In our tumor model, the

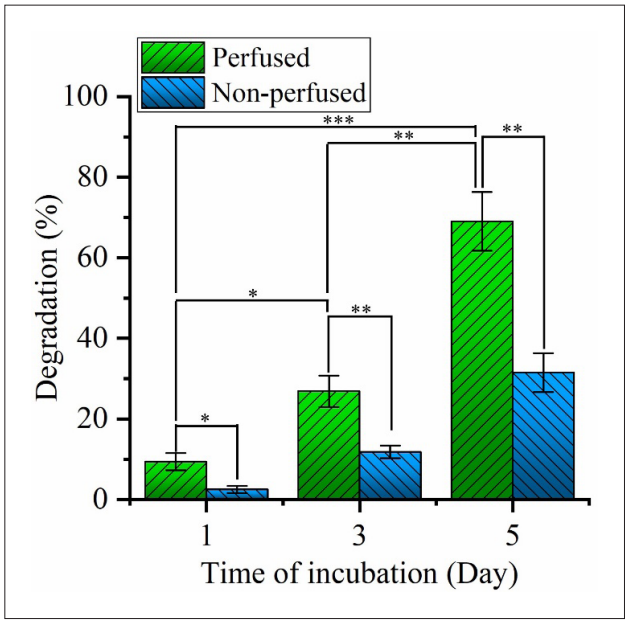

Figure 10. Degradation with increased incubation time for the cell-encapsulated gelatin methacrylate–gelatin hydrogel. Notes: $n = 3$, $^{*}p < 0.05$, $^{**}p < 0.01$, $^{***}p < 0.001$.

initial pore diameter before cell culture was 87 ± 5 μm. After 7 days of culture, the pore diameter increased to 190 ± 8 μm under perfusion, whereas in a non-perfused culture, it reached only 120 ± 4 μm. The greater expansion in the perfused model indicates significantly more extensive matrix degradation, directly attributable to differences in culture conditions. Figure 11 shows the SEM images of the perfusion channel and the microstructure of the hydrogel before and after cell culture. Dynamic medium perfusion through the GelMA–gelatin construct creates a more favorable environment for aggressive tumor cell behavior and ECM remodeling. Studies have shown that perfusion flow led to a several-fold increase in active MMP2 secretion, an enzyme strongly linked to collagen/gelatin degradation and cell migration. This enhanced MMP production accelerates hydrogel breakdown, explaining the large pore enlargement observed after 7 days in our perfused tumor model.[62] Furthermore, the flow of medium imposes fluid shear stress on cells and the matrix, which can serve as a mechanical cue. Tumor cells sense shear forces and often respond by upregulating MMP expression and other remodeling enzymes.[63] In our perfused tumor model, the gentle shear stress from continuous perfusion likely stimulated the cancer cells to secrete more MMPs, accelerating matrix breakdown. This mechanotransduction effect is supported by prior findings that perfusion flow can improve the migratory/invasive phenotype of cancer cells.[40] The robust mass loss and pore enlargement under

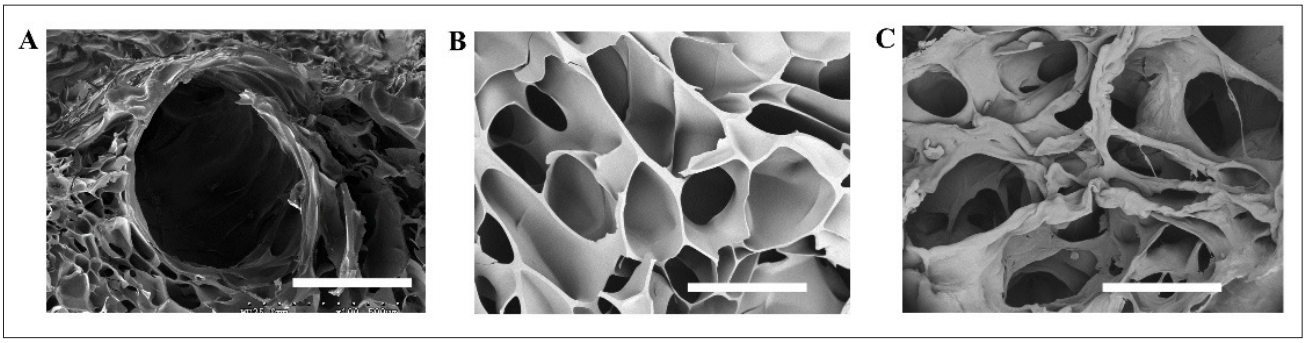

Figure 11. SEM images of the perfusion channel and hydrogel microstruture. (A) Hollow perfusion channel. (B) Hydrogel microstructure before cell culture and (C) degraded hydrogel after cell culture. Scale bar: 300 μm; magnification: 100× for (A) and 180× for (B) and (C).

perfusion demonstrate that our tumor model successfully recapitulates cell-driven ECM degradation, a hallmark of TME remodeling. Moreover, the rapid yet controllable degradation underlines that the GelMA–gelatin system strikes an optimal balance of biocompatibility, enzymatic degradability, and structural support, which is well-suited for simulating the dynamic remodeling processes characteristic of the TME.

We utilized our perfusable 3D tumor model to recapitulate key features of the native TME and investigated the response of SKOV3 ovarian cancer cells to varying concentrations of carboplatin, highlighting the model's utility for chemotherapeutic drug screening. Using a perfusion channel in the tumor construct ensured that it mimicked chemotherapy delivery by a blood vessel in tissues. In less optimized models, gradients in drug penetration can cause variability in cell killing. For instance, in larger static spheroids or hydrogel cultures, cells in the core might evade drug exposure and appear "resistant" due to diffusion limits.[64] By using a flow-through/perfused setup, we minimized those confounding factors, thereby attributing the observed viability differences squarely to cellular phenotypes.

5. Conclusion

This work establishes a perfusable 3D GelMA–gelatin tumor model with a hollow microchannel to interrogate how flow and vascular proximity regulate SKOV3 ovarian cancer cell behavior and chemotherapeutic response. Addressing a key gap in current platforms, our system couples a physiologically scaled, 500 μm perfusable channel with precise, inkjet deposition of tumor cells adjacent to the channel wall, controlled flow (16 μL/min), low shear (0.22 dyn/cm^2), and spatially resolved readouts across concentric regions (0–300, 300–600, and 600–900 μm). Using this integrated design, we quantified distance-dependent changes in morphology, migration, viability, and proliferation under continuous perfusion and contrasted them with static culture.

We found that perfusion significantly enhanced overall cellular function compared to the non-perfused model. After 7 days, cell viability reached 96% in the perfused construct compared to only 71% in the non-perfused counterpart, and the proliferation index was 3.8 in perfused conditions versus 2.2 in non-perfused culture. By dividing the tumor matrix into concentric regions (0–300, 300–600, and 600–900 μm from the channel), we observed a spatial gradient in cell behavior. As the distance from the perfusion channel increased, the cell aspect ratio decreased from 3.5 to 2.45, indicating reduced elongation; migration speed dropped from 28.98 to 21.27 μm/day; and the proliferation index fell from 3.8 to 3.0, highlighting the impact of nutrient and oxygen diffusion limits.

Upon continuous perfusion of carboplatin for 3 days at increasing concentrations (0, 10, 20, and 30 μM), we observed a dose-dependent suppression of cell behavior. Migration speed declined from 28.98 to 4.68 μm/day, proliferation index dropped sharply from 2.3 to 0.46, and cells shifted from elongated to round morphology, with aspect ratio decreasing from 3.15 to 1.17 and circularity increasing from 0.25 to 0.79. Additionally, the perfused model exhibited greater matrix degradation (68% after 5 days of cell culture), with average pore diameter expanding from 87 μm initially to 190 μm after 7 days, compared to only 130 μm in the non-perfused model, suggesting enhanced MMP activity.

Looking ahead, this platform can be further advanced by incorporating endothelial cells to mimic vascular barriers, comparing phenotypic and drug response differences between chemo-naïve and chemo-resistant ovarian cancer subtypes, and investigating synergistic effects of combination chemotherapies within the perfused tumor model. Future studies may include two-dimensional and 3D (perfused and non-perfused) tumor model comparisons, matrix degradation, and molecular

analyses, such as apoptosis and hypoxic markers for deeper mechanistic insights.

Acknowledgments

None.

Funding

None.

Conflict of interest

The authors declare they have no competing interests.

Author contribution

Conceptualization: Md Shahriar, Komaraiah Palle, Changxue Xu
Formal analysis: Md Shahriar, Marielena Molinares, Changxue Xu
Investigation: Md Shahriar, Marielena Molinares
Methodology: Md Shahriar, Komaraiah Palle, Changxue Xu
Writing–original draft: Md Shahriar, Marielena Molinares
Writing–review and editing: Md Shahriar, Ganesh Acharya, Komaraiah Palle, Changxue Xu

Ethics approval and consent to participate

Not applicable.

Consent for publication

Not applicable.

Availability of data

Data is available from the corresponding author upon reasonable request.

References

1. Shi X, Wang X, Yao W, *et al.* Mechanism insights and therapeutic intervention of tumor metastasis: latest developments and perspectives. *Signal Transduct Target Ther*. 2024;9(1):192. doi: 10.1038/s41392-024-01885-2
2. Molinares M, Wolpert N, Gollahon L, Xu C. Effect of micropillar density on morphology and migration of low and high metastatic potential breast cancer cells. *Colloids Surf B Biointerfaces*. 2025;245:114214. doi: 10.1016/j.colsurfb.2024.114214
3. Ge R, Wang Z, Cheng L. Tumor microenvironment heterogeneity an important mediator of prostate cancer progression and therapeutic resistance. *NPJ Precis Oncol*. 2022;6(1):31. doi: 10.1038/s41698-022-00272-w
4. Herrmann D, Conway JR, Vennin C, *et al.* Three-dimensional cancer models mimic cell–matrix interactions in the tumour microenvironment. *Carcinogenesis*. 2014;35(8):1671-1679. doi: 10.1093/carcin/bgu108
5. Cordeiro S, Oliveira BB, Valente R, *et al.* Breaking the mold: 3D cell cultures reshaping the future of cancer research. *Front Cell Dev Biol*. 2024;12:1507388. doi: 10.3389/fcell.2024.1507388
6. Shukla P, Yeleswarapu S, Heinrich MA, Prakash J, Pati F. Mimicking tumor microenvironment by 3D bioprinting: 3D cancer modeling. *Biofabrication*. 2022;14(3):032002. doi: 10.1088/1758-5090/ac6d11
7. Datta P, Dey M, Ataie Z, Unutmaz D, Ozbolat IT. 3D bioprinting for reconstituting the cancer microenvironment. *NPJ Precis Oncol*. 2020;4(1):18. doi: 10.1038/s41698-020-0121-2
8. Gupta D, Derman ID, Xu C, Huang Y, Ozbolat IT. Droplet-based bioprinting. *Nat Rev Methods Primers*. 2025;5(1):25. doi: 10.1038/s43586-025-00394-y
9. Sharifi S, Sharifi H, Akbari A, Chodosh J. Systematic optimization of visible light-induced crosslinking conditions of gelatin methacryloyl (GelMA). *Sci Rep*. 2021; 11(1):23276. doi: 10.1038/s41598-021-02830-x
10. Zhou M, Lee BH, Tan LP. A dual crosslinking strategy to tailor rheological properties of gelatin methacryloyl. *Int J Bioprint*. 2017;3(2):003. doi: 10.18063/IJB.2017.02.003
11. Wang C, Li J, Sinha S, Peterson A, Grant GA, Yang F. Mimicking brain tumor-vasculature microanatomical architecture via co-culture of brain tumor and endothelial cells in 3D hydrogels. *Biomaterials*. 2019;202:35-44. doi: 10.1016/j.biomaterials.2019.02.024
12. Ertekin Ö, Monavari M, Krueger R, *et al.* 3D hydrogel-based microcapsules as an in vitro model to study tumorigenicity, cell migration and drug resistance. *Acta Biomater*. 2022;142:208-220. doi: 10.1016/j.actbio.2022.02.010
13. Maggiotto F, Bova L, Micheli S, *et al.* 3D bioprinting for the production of a perfusable vascularized model of a cancer niche. *Front Bioeng Biotechnol*. 2025;13:1484738. doi: 10.3389/fbioe.2025.1484738
14. Hong M, Hong S, Song JM. 3D bioprinted multidrug resistance (MDR)-dependent tumor spheroids. *ACS Appl Mater Interfaces*. 2025;17(5):7377-7394. doi: 10.1021/acsami.4c19291
15. Fang T, Xie X, Lu W, *et al.* Patient-derived organoids on a microarray for drug resistance study in breast cancer. *Anal Chem*. 2024;96(46):18384-18391. doi: 10.1021/acs.analchem.4c02691
16. Krishnamoorthy S, Wadnap S, Noorani B, Xu H, Xu C. Investigation of gelatin methacrylate working curves in

dynamic optical projection stereolithography of vascular-like constructs. *Eur Polym J*. 2020;124:109487.
doi: 10.1016/j.eurpolymj.2020.109487

17. Ren B, Song K, Sanikommu AR, *et al.* Study of sacrificial ink-assisted embedded printing for 3D perfusable channel creation for biomedical applications. *Appl Phys Rev*. 2022;9(1):011408.
doi: 10.1063/5.0068329

18. Schmolka IR. Artificial skin I. Preparation and properties of pluronic F-127 gels for treatment of burns. *J Biomed Mater Res*. 1972;6(6):571-582.
doi: 10.1002/jbm.820060609

19. Liu J, Xu C. Improving uniformity of cell distribution in post-inkjet-based bioprinting. *J Manuf Sci Eng*. 2024;146(1):014501.
doi: 10.1115/1.4063134

20. Liu J, Xu H, Shahriar M, Xu C. Modeling of cell distribution dynamics in cell-laden bioink with active circulation. *Addit Manuf*. 2023;73:103669.
doi: 10.1016/j.addma.2023.103669

21. Xu H, Liu J, Shahriar M, and Xu C. Investigation of cell aggregation on the printing performance in inkjet-based bioprinting of cell-laden bioink. *Langmuir*. 2022;39(1):545-555.
doi: 10.1021/acs.langmuir.2c02817

22. Hyler AR, Baudoin NC, Brown MS, *et al.* Fluid shear stress impacts ovarian cancer cell viability, subcellular organization, and promotes genomic instability. *PLoS One*. 2018;13(3):e0194170.
doi: 10.1371/journal.pone.0194170.

23. Galpayage Dona KNU, Hale JF, Salako T, *et al.* The use of tissue engineering to fabricate perfusable 3D brain microvessels in vitro. *Front Physiol*. 2021;12:715431.
doi: 10.3389/fphys.2021.715431.

24. Nichol JW, Koshy ST, Bae H, Hwang CM, Yamanlar S, Khademhosseini A. Cell-laden microengineered gelatin methacrylate hydrogels. *Biomaterials*. 2010;31(21):5536-5544.
doi: 10.1016/j.biomaterials.2010.03.064.

25. Zhao X, Lang Q, Yildirimer L, *et al.* Photocrosslinkable gelatin hydrogel for epidermal tissue engineering. *Adv Healthc Mater*. 2016;5(1):108-118.
doi: 10.1002/adhm.201500005.

26. Krishnamoorthy S, Noorani B, Xu C. Effects of encapsulated cells on the physical–mechanical properties and microstructure of gelatin methacrylate hydrogels. *Int J Mol Sci*. 2019;20(20):5061.
doi: 10.3390/ijms20205061.

27. Friedl P, Wolf K. Tumour-cell invasion and migration: diversity and escape mechanisms. *Nat Rev Cancer*. 2003;3(5):362-374.
doi: 10.1038/nrc1075.

28. Helmy IM, AbdelAzim AM. Efficacy of ImageJ in the assessment of apoptosis. *Diagn Pathol*. 2012;7(1):15.
doi: 10.1186/1746-1596-7-15.

29. Liu J, Xu C. Spatial distribution of encapsulated cells dramatically alters biomechanical properties and microstructure of 3D printed cellular structures. *J Manuf Processes*. 2024;120:1203-1212.
doi: 10.1016/j.jmapro.2024.05.029.

30. Figueiredo L, Leisage C, Weiss P, Yang J. Quantifying oxygen levels in 3D bioprinted cell-laden thick constructs with perfusable microchannel networks. *Polymers*. 2020;12(6):1260.
doi: 10.3390/polym12061260.

31. Radisic M, Malda J, Epping E, Geng W, Langer R, Vunjak-Novakovic G. Oxygen gradients correlate with cell density and cell viability in engineered cardiac tissue. *Biotechnol Bioeng*. 2006;93(2):332-343.
doi: 10.1002/bit.20722.

32. Novak CM, Horst EN, Taylor CC, Liu CZ, Mehta G. Fluid shear stress stimulates breast cancer cells to display invasive and chemoresistant phenotypes while upregulating PLAU in a 3D bioreactor. *Biotechnol Bioeng*. 2019; 116(11):3084-3097.
doi: 10.1002/bit.27119.

33. Helmlinger G, Yuan F, Dellian M, Jain RK. Interstitial pH and pO2 gradients in solid tumors in vivo: high-resolution measurements reveal a lack of correlation. *Nat Med*. 1997;3(2):177-182.
doi: 10.1038/nm0297-177.

34. Liverani C, De Vita A, Minardi S, *et al.* A biomimetic 3D model of hypoxia-driven cancer progression. *Sci Rep*. 2019;9(1):12263.
doi: 10.1038/s41598-019-48701-4.

35. Lewis DM, Park KM, Tang V, *et al.* Intratumoral oxygen gradients mediate sarcoma cell invasion. *Proc Natl Acad Sci USA*. 2016;113(33):9292-9297.
doi: 10.1073/pnas.1605317113.

36. Polacheck WJ, German AE, Mammoto A, Ingber DE, Kamm RD. Mechanotransduction of fluid stresses governs 3D cell migration. *Proc Natl Acad Sci USA*. 2014;111(7):2447-2452.
doi: 10.1073/pnas.1316848111.

37. Avraham-Chakim L, Elad D, Zaretsky U, Kloog Y, Jaffa A, Grisaru D. Fluid-flow induced wall shear stress and epithelial ovarian cancer peritoneal spreading. *PLoS One*. 2013;8(4):e60965.
doi: 10.1371/journal.pone.0060965.

38. Gilmore AC, Flaherty SJ, Somasundaram V, *et al.* An in vitro tumorigenesis model based on live-cell-generated oxygen and nutrient gradients. *Commun Biol*. 2021;4(1):477.
doi: 10.1038/s42003-021-01954-0.

39. Chen Z, Han F, Du Y, Shi H, Zhou W. Hypoxic microenvironment in cancer: molecular mechanisms

and therapeutic interventions. *Signal Trans Targeted Ther.* 2023;8(1):70.
doi: 10.1038/s41392-023-01332-8.

40. Pasini A, Lovecchio J, Cortesi M, *et al.* Perfusion flow enhances viability and migratory phenotype in 3D-cultured breast cancer cells. *Ann Biomed Eng.* 2021;49(9):2103-2113.
doi: 10.1007/s10439-021-02727-w.

41. Worsley CM, Veale RB, Mayne ES. The acidic tumour microenvironment: manipulating the immune response to elicit escape. *Hum Immunol.* 2022;83(5):399-408.
doi: 10.1016/j.humimm.2022.01.014.

42. Tannock IF. Oxygen diffusion and the distribution of cellular radiosensitivity in tumours. *Br J Radiol.* 1972;45(535):515-524.
doi: 10.1259/0007-1285-45-535-515.

43. Ayuso JM, Virumbrales-Munoz M, McMinn PH, *et al.* Tumor-on-a-chip: a microfluidic model to study cell response to environmental gradients. *Lab Chip.* 2019;19(20):3461-3471.
doi: 10.1039/c9lc00270g.

44. Lee D, Jeong HS, Hwang SY, Lee YG, Kang YJ. ABCB1 confers resistance to carboplatin by accumulating stem-like cells in the G2/M phase of the cell cycle in p53null ovarian cancer. *Cell Death Discov.* 2025;11(1):132.
doi: 10.1038/s41420-025-02435-7.

45. Alhalhooly L, Mamnoon B, Kim J, Mallik S, Choi Y. Dynamic cellular biomechanics in responses to chemotherapeutic drug in hypoxia probed by atomic force spectroscopy. *Oncotarget.* 2021;12(12):1165.
doi: 10.18632/oncotarget.27974.

46. Povea-Cabello S, Oropesa-Ávila M, De la Cruz-Ojeda P, *et al.* Dynamic reorganization of the cytoskeleton during apoptosis: the two coffins hypothesis. *Int J Mol Sci.* 2017;18(11):2393.
doi: 10.3390/ijms18112393.

47. He PJ, Ge RF, Mao WJ, *et al.* Oxidative stress induced by carboplatin promotes apoptosis and inhibits migration of HN-3 cells. *Oncol Lett.* 2018;16(6):7131-7138.
doi: 10.3892/ol.2018.9563.

48. Alamdari SG, Mohammadzadeh R, Amini M, *et al.* Improvement of carboplatin chemosensitivity in lung cancer cells by siRNA-mediated downregulation of DLGAP1-AS2 expression. *Sci Rep.* 2025; 15(1):7971.
doi: 10.1038/s41598-025-87649-6.

49. Vaidžiulytė K, Macé AS, Battistella A, Beng W, Schauer K, Coppey M. Persistent cell migration emerges from a coupling between protrusion dynamics and polarized trafficking. *Elife.* 2022;11:e69229.
doi: 10.7554/eLife.69229.

50. Shields JD, Fleury ME, Yong C, *et al.* Autologous chemotaxis as a mechanism of tumor cell homing to lymphatics via interstitial flow and autocrine CCR7 signaling. *Cancer Cell.* 2007;11(6):526-538.
doi: 10.1016/j.ccr.2007.04.020.

51. Waldeland JO, Evje S. Competing tumor cell migration mechanisms caused by interstitial fluid flow. *J Biomech.* 2018;81:22-35.
doi: 10.1016/j.jbiomech.2018.09.011.

52. Nath S, Pigula M, Khan AP, *et al.* Flow-induced shear stress confers resistance to carboplatin in an adherent three-dimensional model for ovarian cancer: a role for EGFR-targeted photoimmunotherapy informed by physical stress. *J Clin Med.* 2020;9(4):924.
doi: 10.3390/jcm9040924.

53. Banerji U, Sain N, Sharp SY, *et al.* An in vitro and in vivo study of the combination of the heat shock protein inhibitor 17-allylamino-17-demethoxygeldanamycin and carboplatin in human ovarian cancer models. *Cancer Chemother Pharmacol.* 2008;62(5):769-778.
doi: 10.1007/s00280-007-0662-x.

54. Sousa GFD, Wlodarczyk SR, Monteiro G. Carboplatin: molecular mechanisms of action associated with chemoresistance. *Braz J Pharm Sci.* 2014;50(4):693-701.
doi: 10.1590/S1984-82502014000400004.

55. Patra B, Lateef MA, Brodeur MN, *et al.* Carboplatin sensitivity in epithelial ovarian cancer cell lines: the impact of model systems. *PLoS One.* 2020;15(12):e0244549.
doi: 10.1371/journal.pone.0244549.

56. Lieberthal TJ, Sahakyants T, Szabo-Wexler NR, *et al.* Implantable 3D printed hydrogels with intrinsic channels for liver tissue engineering. *Proc Natl Acad Sci U S A.* 2024;121(47):e2403322121.
doi: 10.1073/pnas.2403322121.

57. Zhang N, Qavi I, Halder S, Tan G. Biomimetic hydrogel scaffolds embedded with porous microtubes as perfusion channels. *Manuf Lett.* 2023;35:184-193.
doi: 10.1016/j.mfglet.2023.08.009.

58. Grebenyuk S, Abdel Fattah AR, Kumar M, *et al.* Large-scale perfused tissues via synthetic 3D soft microfluidics. *Nat Commun.* 2023;14(1):193.
doi: 10.1038/s41467-022-35619-1.

59. Blanco-Fernandez B, Gaspar VM, Engel E, Mano JF. Proteinaceous hydrogels for bioengineering advanced 3D tumor models. *Adv Sci (Weinh).* 2021;8(4):2003129.
doi: 10.1002/advs.202003129

60. Zhu M, Wang Y, Ferracci G, Zheng J, Cho NJ, Lee BH. Gelatin methacryloyl and its hydrogels with an exceptional degree of controllability and batch-to-batch consistency. *Sci Rep.* 2019;9(1):6863.
doi: 10.1038/s41598-019-42186-x

61. Didwischus N, Guduru A, Badylak SF, Modo M. In vitro dose-dependent effects of matrix metalloproteinases on ECM hydrogel biodegradation. *Acta Biomater.* 2024;174:104-115.

doi: 10.1016/j.actbio.2023₹.12.003

62. Saggioro M, D'Agostino S, Veltri G, *et al.* A perfusion-based three-dimensional cell culture system to model alveolar rhabdomyosarcoma pathological features. *Sci Rep*. 2023;13(1):9444.
doi: 10.1038/s41598-023-36210-4

63. Huang Q, Hu X, He W, *et al.* Fluid shear stress and tumor metastasis. *Am J Cancer Res*. 2018;8(5):763-775.

64. Marrella A, Varani G, Aiello M, *et al.* 3D fluid-dynamic ovarian cancer model resembling systemic drug administration for efficacy assay. *Altex*. 2021;38(1):82-94.
doi: 10.14573/altex.2003131